

Article

Structural, Thermal and Functional Properties of a Hybrid Dicyanamide-Perovskite Solid Solution

Javier García-Ben ^{1,2}, Jorge Salgado-Beceiro ^{1,2}, Ignacio Delgado-Ferreiro ^{1,2}, Pedro Dafonte-Rodríguez ^{1,2}, Jorge López-Beceiro ³, Ramón Artiaga ³, Socorro Castro-García ^{1,2}, Manuel Sánchez-Andújar ^{1,2}, Juan Manuel Bermúdez-García ^{1,2,*} and María Antonia Señaris-Rodríguez ^{1,2,*}

- ¹ Quimolmat, Centro de Investigaciones Científicas Avanzadas (CICA), Universidade da Coruña, Rúa as Carballeiras, 15071 A Coruña, Spain; javier.garcia.ben@udc.es (J.G.-B.); jorge.salgado@udc.es (J.S.-B.); ignacio.delgado.ferreiro@udc.es (I.D.-F.); pedro.dafonte.rodriguez@udc.es (P.D.-R.); socorro.castro.garcia@udc.es (S.C.-G.); m.andujar@udc.es (M.S.-A.)
- ² Quimolmat, Departamento de Química, Facultade de Ciencias, Universidade da Coruña, Campus da Zapateira, 15008 A Coruña, Spain
- ³ Escuela Politécnica de Ingeniería de Ferrol, Universidade da Coruña, Campus Industrial de Ferrol, 15403 Ferrol, Spain; jorge.lopez.beceiro@udc.es (J.L.-B.); ramon.artiaga@udc.es (R.A.)
- * Correspondence: j.bermudez@udc.es (J.M.B.-G.); m.senaris.rodriguez@udc.es (M.A.S.-R.)



Citation: García-Ben, J.; Salgado-Beceiro, J.; Delgado-Ferreiro, I.; Dafonte-Rodríguez, P.; López-Beceiro, J.; Artiaga, R.; Castro-García, S.; Sánchez-Andújar, M.; Bermúdez-García, J.M.; Señaris-Rodríguez, M.A. Structural, Thermal and Functional Properties of a Hybrid Dicyanamide-Perovskite Solid Solution. *Crystals* **2022**, *12*, 860. <https://doi.org/10.3390/cryst12060860>

Academic Editors: Maria Gazda, Jesús Prado-Gonjal, Beatriz Molero-Sánchez and Sara A. López-Paz

Received: 30 April 2022

Accepted: 13 June 2022

Published: 18 June 2022

Publisher's Note: MDPI stays neutral with regard to jurisdictional claims in published maps and institutional affiliations.



Copyright: © 2022 by the authors. Licensee MDPI, Basel, Switzerland. This article is an open access article distributed under the terms and conditions of the Creative Commons Attribution (CC BY) license (<https://creativecommons.org/licenses/by/4.0/>).

Abstract: In Solid-State Chemistry, a well-known route to obtain new compounds and modulate their properties is the formation of solid solutions, a strategy widely exploited in the case of classical inorganic perovskites but relatively unexplored among emergent hybrid organic–inorganic perovskites (HOIPs). In this work, to the best of our knowledge, we present the first dicyanamide-perovskite solid solution of [TPrA][Co_{0.5}Ni_{0.5}(dca)₃] and study its thermal, dielectric and optical properties, comparing them with those of the parent undoped compounds [TPrA][Co(dca)₃] and [TPrA][Ni(dca)₃]. In addition, we show that the prepared doped compound can be used as a precursor that, by calcination, allows CNTs with embedded magnetic Ni:Co alloy nanoparticles to be obtained through a fast and much simpler synthetic route than other complex CVD or arc-discharge methods used to obtain this type of material.

Keywords: hybrid perovskites; solid solution; dielectric properties; phase transition

1. Introduction

In recent years, the family of hybrid organic–inorganic perovskites (HOIPs) has arisen as a spin-off of traditional inorganic perovskites [1], and they are gaining increasing interest within the scientific community owing to their interesting functional and multifunctional properties [2], such as ferroic and multiferroic properties [3–7], unprecedented photoconductivity for solar cells [8,9] and giant barocaloric effects for eco-friendly refrigeration [10–12].

Similar to their inorganic predecessors, hybrid perovskites exhibit the general formula ABX₃, where [BX₆] octahedra are linked by their corners through X anions, forming pseudocuboctahedra cavities that accommodate A cations. In the case of inorganic perovskites, A is generally an alkaline or alkaline-earth metal cation, B is normally a transition-metal cation, and X can be different types of monoatomic anions, such as oxygen, nitride, sulfide and/or halide anions. Meanwhile, in hybrid perovskites, the A cation is replaced by large organic cations (such as alkylammonium or alkylphosphonium), and X can remain as a halide anion or, more often, is replaced by a polyatomic ligand (such as formate, cyanide, azide or dicyanamide, among others) [1].

From the chemical and structural point of view, it is well known that traditional inorganic perovskites are highly tolerant to partial and/or total substitution of the A, B and X building blocks, leading to so-called substitutional solid solutions [13].

Over the years, this strategy has successfully allowed the modulation, tuning and even introduction of new functional properties in inorganic perovskites, such as high-temperature superconductivity [14] and colossal magnetoresistance [15].

Nevertheless, studies on solid solutions in analogous hybrid perovskites are still scarce and mainly limited to perovskites with short ligands, such as halides, formates or hypophosphites [16–18]. One example is the work of Cheetham et al., who were able to obtain mixed X-site perovskites using formate and hypophosphite ligands on [GUA][Mn(HCOO)_{3-x}(H₂POO)_x] (GUA = guanidinium cation) [19]. Another example is Goodwin et al.'s work, who reported the synthesis and structural characterization of three mixed-metal formate perovskite families [C(NH₂)₃][Cu_xM_{1-x}(HCOO)₃] (M = Mn, Zn, Mg). Very interestingly, for $x = 0.5$, these authors reported nanoscale segregation involving the coexistence of polar/apolar nanoregions, such as relaxor ferroelectrics [20]. In any case, this approach offers a valuable new handle for controlling the properties of hybrid perovskites, opening the door to many new possible compositions. In this context, it should be noted that the preparation of hybrid perovskite solid solutions by either cation or anion substitution remains a challenge due to several factors. On the one hand, the large differences between the sizes of some anions and others make it difficult to obtain X-site substituted solutions [21]. On the other hand, the fact that there is more variability in cations than anions makes it difficult to find the right anion/cation combination without compromising structural stability [21]. Moreover, differences in the kinetics of crystal growth with different cations or anions can arise, with one of the structures being more favored [22].

In the particular case of dicyanamide-perovskites with the general formula [A][M(dca)₃] (dca = (CN)₂N⁻), some interesting properties arise due to the length and flexibility of the dicyanamide anion [23]. Such flexibility gives rise to pseudo-cubic cavities that can be modulable in size and shape to accommodate a wide diversity of A-cations. Actually, the variability in the size of the A-cations that can form this hybrid perovskite is the largest within the HOIP family. Moreover, these structures tolerate a large diversity of transition-metal cations M in the B-site, such as Mn²⁺, Ni²⁺, Co²⁺, Fe²⁺ or Cd²⁺. Very interesting properties found in this family of hybrids, such as magnetic and dielectric properties, large pressure responsiveness and even giant barocaloric effects, are given by structural characteristics, which can be tuned by selecting different building blocks [23–28].

However, despite the intensive studies on the family of dicyanamide-perovskites in recent years, to the best of our knowledge, no studies have been reported that address the use of solid solutions to tune their crystal structures and functional properties.

In this work, we report the preparation and structural characterization of a substitutional solid solution with Co:Ni = 1:1 in the M position of the previously reported [TPrA][M(dca)₃] perovskite (TPrA = (CH₃CH₂CH₂)₄N⁺; M = Ni²⁺, Co²⁺; dca = (N(CN)₂)⁻) [24]. We also report the variations in the dielectric, optical and thermal properties of the parent hybrid perovskites with the formation of this solid solution.

In addition, given the ability of the original hybrids to give rise to metal nanoparticle systems embedded in carbon nanotubes by controlled calcination [29], we studied the potential of the solid solution to also be used as a precursor for carbon nanostructures.

2. Materials and Methods

2.1. Materials and Synthesis

Commercially available Co(NO₃)₂·6H₂O (98%, Sigma-Aldrich), Ni(NO₃)₂·6H₂O (Z98.5%, Sigma-Aldrich), (TPrA)Br (98%, Aldrich), Na(dca) (96%, Aldrich) and absolute ethanol (Pan-reac) were employed.

The synthetic route followed for the preparation of [TPrA][Co_{0.5}Ni_{0.5}(dca)₃] was the slow evaporation of a mixture of all reagents (see Figure S1). Four different solutions of 2 mmol of (TPrA)Br solved in 20 mL of absolute ethanol, 6 mmol of Na(dca) in 10 mL of H₂O, 1 mmol of Co(NO₃)₂·6H₂O in 5 mL of H₂O and 1 mmol of Ni(NO₃)₂·6H₂O in 5 mL of H₂O were prepared separately. Ni and Co solutions were mixed together; dca and the

TPrA solutions were also mixed together; and finally, both resultant solutions were mixed in a crystallizer. After two days, small cubic purple crystals (around 1 mm) were formed, isolated by filtration and washed several times with ethanol.

Part of the obtained product was thermally decomposed in order to check its ability to be used as a precursor of metal and carbon nanostructures, following the method reported by J.M. Bermudez-Garcia et al. [29]. The sample was heated in a tubular furnace (Lenton LTF 16/–/180) under a nitrogen atmosphere at 5 °C/min from room temperature up to 900 °C, maintaining that temperature for 1 h and then cooling it down at 10 °C/min.

2.2. Powder X-ray Diffraction

A Siemens D-5000 diffractometer using $\text{CuK}\alpha$ radiation ($\lambda = 1.5418 \text{ \AA}$) was used to study the compounds by X-ray powder diffraction (XRPD) at room temperature. The PXRD pattern was refined with the Le Bail method using the software GSAS-II version 5046.

2.3. Single-Crystal X-ray Diffraction

Single-crystal X-ray diffraction data were collected at 100 K in a Bruker-Nonius x8 ApexII X-ray diffractometer equipped with a CCD detector and using monochromatic $\text{MoK}\alpha_1$ radiation ($\lambda = 0.71073 \text{ \AA}$). For this experiment, a suitable crystal was chosen and mounted on a glass fiber using instant glue. The crystal was cooled at a rate of 10 K/min using a cold stream of nitrogen from a Kyroflex cryostream cooler. Data integration and reduction were performed using the Apex2 V.1.0-27 (Bruker Nonius, 2005) suite software. The intensity collected was corrected for Lorentz and polarization effects and for absorption by semiempirical methods on the basis of symmetry-equivalent data using SADABS (2004) of the suite software. The structure was solved by the dual-space algorithm implemented in the SHELXT2014/5 program and was refined by the least-squares method on SHELXL2018/3.

2.4. Differential Scanning Calorimetry (DSC)

Differential scanning calorimetric (DSC) analysis measurements from 200 K to 390 K were carried out using a TA-Instruments Q2000 with an RCS 90 cooler, heated and cooled at a rate of 20 K min^{-1} under a nitrogen atmosphere, using around 20 mg of sample.

2.5. Thermogravimetric Analysis (TGA)

Thermogravimetric analysis (TGA) was carried out in a simultaneous TGA-DTA analyzer (SDT2960) at a rate of 10 K min^{-1} from 25 to 1000 K under a nitrogen atmosphere using around 17 mg of sample.

2.6. Dielectric Measurements

The complex dielectric permittivity ($\epsilon_r = \epsilon_r' - i\epsilon_r''$) of the cold-press pelletized samples was measured as a function of frequency and temperature with a parallel-plate capacitor coupled to a Solartron 1260A Impedance/Gain-Phase Analyzer, capable of measuring in the frequency range from 10 mHz to 32 MHz using an amplitude of 2 V. The capacitor was mounted in a Janis SVT200T cryostat refrigerated with liquid nitrogen and with a Lakeshore 332 incorporated to control the temperature from 150 to 400 K. Data were collected upon heating.

Pelletized samples, made from cold-press non-oriented single crystals with an area of approximately 133 mm^2 and a thickness of approximately 1.3 mm, were prepared to fit into the capacitor, and gold was sputtered on their surfaces to ensure good electrical contact with the electrodes.

All dielectric measurements were carried out in a nitrogen atmosphere, where several cycles of vacuum and nitrogen gas were performed to ensure that the sample environment was free of water.

2.7. Ultraviolet–Visible (U-VIS) Spectroscopy

Optical diffuse-reflectance measurements of powders were performed at room temperature using a Jasco V-650 UV–Visible double-beam spectrophotometer with single monochromators operating from 200 to 800 nm. BaSO₄ was used as a non-absorbing reflectance reference.

2.8. Scanning Electron Microscopy (SEM) and Energy-Dispersive X-ray Spectroscopy (EDS)

The morphology of the samples was analyzed using a JEOL JSM-7200F Schottky field-emission scanning electron microscope (FE-SEM). Chemical analyses were carried out using JEOL JSM-7200F equipped with an Oxford Instruments X-Max detector for energy-dispersive X-ray spectroscopy (EDS).

2.9. Transmission Electron Microscopy (TEM)

The morphology and the microstructure of the samples were tested by transmission electron microscopy (TEM) in a JEOL TEM-1010 operating at 100 kV and equipped with a Gatan Rio camera.

3. Results and Discussion

3.1. Compositional and Structural Characterization

We synthesized the doped sample [TPrA][Co_{0.5}Ni_{0.5}(dca)₃], as well as the parent hybrid perovskites, [TPrA][Co(dca)₃] and [TPrA][Ni(dca)₃], in order to study the crystal structure and various functional properties of the new Co:Ni = 1:1 material and to compare it with the unsubstituted perovskites prepared in an analogous way. For this purpose, we prepared the three systems by adapting the method described in the literature [24,25] (see Section 2). In this way, we obtained cubic-shaped single crystals of different colors depending on the Co:Ni ratio with sizes between 2 and 1.5 mm (see Figure 1).



Figure 1. Cubic single crystals of [TPrA][Co_xNi_{1-x}(dca)₃], where $x = 1.0, 0.5$ and 0.0 .

3.1.1. Energy-Dispersive X-ray Spectroscopy (EDS) Results

In order to corroborate the proportion of each metal in the doped sample, we performed energy-dispersive X-ray spectroscopy (EDS) analysis (see Figure S2a). Figures S2 and S3 show, respectively, the EDS spectrum and mapping of the sample denoted [TPrA][Co_{0.5}Ni_{0.5}(dca)₃]. The obtained data reveal the presence of both Ni and Co in similar proportions (48.8% Co and 51.2% Ni) with a homogeneous distribution at the microscale.

3.1.2. Powder X-ray Diffraction

The X-ray diffraction patterns at room temperature (see Figure 2a) show that the doped sample was obtained as a pure sample, and that it actually presents the same crystal

structure as that already described for unsubstituted perovskites at the same temperature (from now on, called “polymorph Ib”, by analogy with the parent compounds) [24]. Figure 2b shows the details of the most intense peak, in the 2θ region of $14\text{--}17^\circ$, where it can be clearly seen that: (i) the maximum is not split in the compound with Co:Ni = 1:1, and (ii) there is a regular displacement of the position of this maximum towards larger angles as the amount of nickel increases. This is an indication that, at the scale seen by PXRD, a solid solution is formed, and no phase segregation is observed. Zooming in on many other maxima shows analogous behavior.

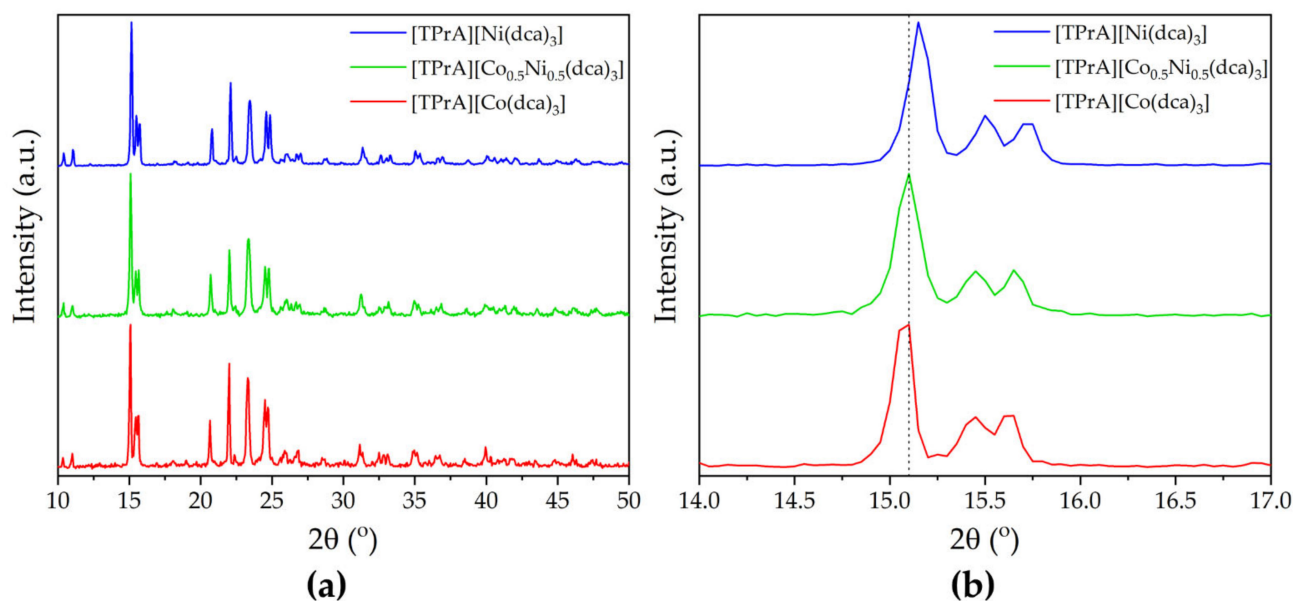


Figure 2. (a) Powder X-ray diffraction patterns of $[\text{TPrA}][\text{Co}_x\text{Ni}_{1-x}(\text{dca})_3]$, where $x = 1.5, 0.5$ and 0.0 . (b) Details of a region of (a) to show the shape and the shift of the peak as x changes.

Additionally, the obtained patterns were analyzed using Le Bail refinement (see Figures 3 and S4), which shows good agreement between the proposed model and the experimental patterns. It is worth noting that the $[\text{TPrA}][\text{Co}_{0.5}\text{Ni}_{0.5}(\text{dca})_3]$ pattern could be satisfactorily refined as a single phase without any evidence of phase segregation. It has orthorhombic symmetry with the space group $Pnna$ and lattice parameters $a = 17.2330(17)$ Å, $b = 23.0758(20)$ Å and $c = 22.7800(19)$ Å. Figure 3 shows the evolution of the $[\text{TPrA}][\text{Co}_{1-x}\text{Ni}_x(\text{dca})_3]$ lattice parameters and volume obtained from the Le Bail refinements versus the Ni content. We can observe that the lattice parameters and volume clearly decrease upon Ni doping, which can be related to the smaller size of Ni^{2+} compared to Co^{2+} cations (0.69 Å versus 0.745 Å, respectively) [30].

3.1.3. Single-Crystal X-ray Diffraction

In order to further analyze the crystal structure of $[\text{TPrA}][\text{Co}_{0.5}\text{Ni}_{0.5}(\text{dca})_3]$, we also performed single-crystal X-ray diffraction at low temperature. The studies carried out at $T = 100$ K show that $[\text{TPrA}][\text{Co}_{0.5}\text{Ni}_{0.5}(\text{dca})_3]$ crystallizes with tetragonal symmetry with the space group $P4_21c$ (non-centrosymmetric) and cell parameters $a = 16.065(1)$ Å and $c = 17.055(1)$ Å (see Table S1 for more details). It is worth noting that this low-temperature crystal structure is different to that obtained for this composition by PXRD at room temperature and analogous to the low-temperature crystal structure of the parent compounds [24].

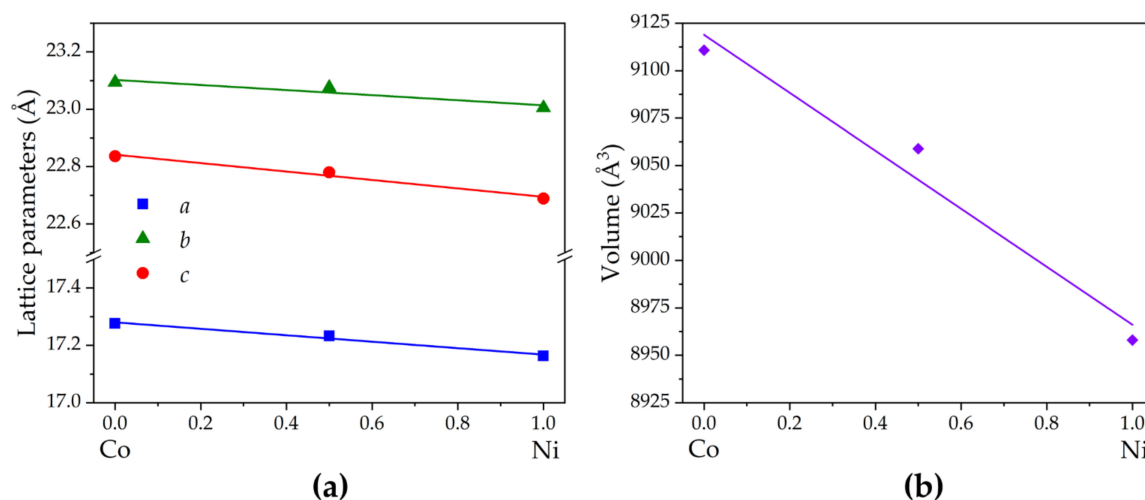


Figure 3. (a) Lattice parameters and (b) unit cell volume for $[\text{TPrA}][\text{Co}_x\text{Ni}_{1-x}(\text{dca})_3]$, where $x = 1.0, 0.5$ and 0.0 .

The asymmetric unit of this low-temperature polymorph (from now on, called “polymorph I”, by analogy with the parent compounds) contains one independent metal cation, three dca anions and three TPrA cations. Both Co^{2+} and Ni^{2+} cations are randomly distributed in a single crystallographic site and connected to their six nearest neighbors through six $\mu_{1,5}$ -dca bridges in a distorted octahedral environment, with six different M–N distances (see Table S2). The resulting $[\text{MN}_6]$ octahedra are cooperatively rotated along the main crystallographic axes (tilt systems $a^-b^+c^-$ in Glazer notation). The metal cations and dca anions build a 3D framework with cuboctahedral cavities, which are occupied by TPrA cations. Additionally, this crystal structure exhibits some disorder in the N-amide atoms and C atoms of the dca anions, as well as in the C atom positions of half of the TPrA cations. The here-obtained structural data for this mixed compound are summarized in Table S1 and Figure 4. All of those structural findings are in agreement with those previously reported in the literature for the parent compounds of Ni^{2+} and Co^{2+} . The values of the cell parameters fit between those of the parent hybrids and confirm the regular decrease in the unit cell size with increasing Ni:Co ratio, analogous to what was observed for the polymorph at room temperature.

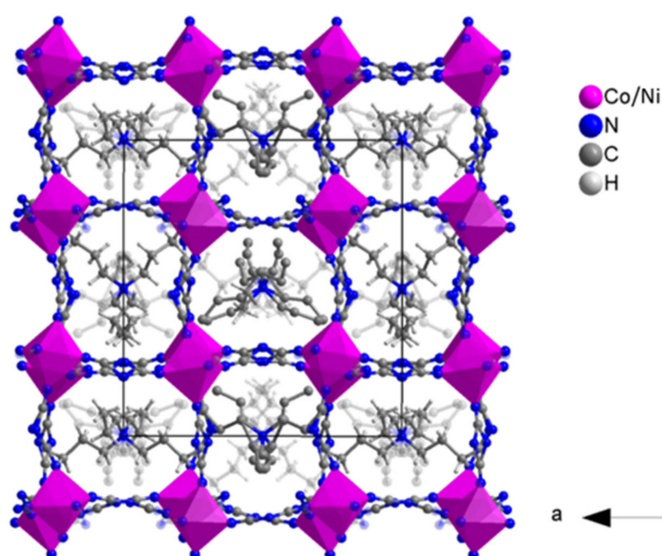


Figure 4. A polyhedral/ball-and-stick representation of the crystal structure of $[\text{TPrA}][\text{Co}_{0.5}\text{Ni}_{0.5}(\text{dca})_3]$ polymorph I (T = 100 K) along the b -axis.

3.2. Thermal Properties

Given that the parent dicyanamide-perovskites, [TPrA][Co(dca)₃] and [TPrA][Ni(dca)₃], present multiple structural phase transitions in the 100–370 K interval, and these transitions are associated with enthalpy and entropy changes of interest for cooling applications [24], we performed differential scanning calorimetry (DSC) and thermogravimetric (TGA) analysis of [TPrA][Co_{0.5}Ni_{0.5}(dca)₃] in order to check the thermal properties of the new solid solution.

As expected, the DSC results (Figure 5) showed three phase transitions upon heating and cooling for [TPrA][Co_{0.5}Ni_{0.5}(dca)₃], which can be related to four different polymorphs, named I, Ia, Ib and II, in order of increasing temperature, analogous to the data reported for the parent compounds [24] (also compared in Figure 5 and in more detail in Figure S5). Assuming the analogy, we suggest that the first endothermic peak upon heating corresponds to the transition polymorph I → polymorph Ia and is found at T₁ = 227.7 K with a total enthalpy of 2.99 J/g and a total entropy of 13.13 J/K kg for the solid solution. Unfortunately, the corresponding peak upon cooling cannot be found due to instrumental limitations in controlling the temperature in this region. The second transition, polymorph Ia → polymorph Ib, can be seen at T₂ = 300.8 K upon heating and 289.5 K upon cooling, with enthalpies of 2.59 J/g and 2.24 J/g and entropies of 8.61 J/K kg and 7.74 J/K kg, respectively. The high-temperature transition, polymorph Ib → polymorph II, appears at T₃ = 347.4 K upon heating and 347.3 K upon cooling with enthalpy and entropy changes of 4.79 J/g and 4.74 J/g and 13.79 J/K kg and 13.65 J/K kg, respectively. These values are compared with those reported for the parent compounds in Table 1 and also in Figure S6, where the transition temperatures are represented versus Ni content. As can be seen there, very interestingly: (i) in the case of the first transition (polymorph I → polymorph Ia), there is a clear metal content dependence on the transition temperature, the enthalpy and the entropy; (ii) the second transition (polymorph Ia → polymorph Ib) is almost independent of the metal content; and (iii) in the case of the third transition (polymorph Ib → polymorph II), the transition temperature clearly depends on the metal content, while the enthalpy and entropy show a low dependence on this factor. It should be noted that, in all cases, the values for the mixed sample are always between the values of the parent compounds, in line with the expected behavior for a solid solution. Nevertheless, the low-temperature transition of the Ni compound exhibits a dramatic decrease in the enthalpy change, whose origin still remains unclear, requiring further studies to clarify it.

Table 1. Thermal parameters of [TPrA][Co_{1-x}Ni_x(dca)₃] (x = 0.0, 0.5 and 1.0). Note: H = on heating, C = on cooling.

Metal	T ₁ (K)	ΔH ₁ (J g ⁻¹)	ΔS ₁ (J K ⁻¹ kg ⁻¹)	T ₂ (K)	ΔH ₂ (J g ⁻¹)	ΔS ₂ (J K ⁻¹ kg ⁻¹)	T ₃ (K)	ΔH ₃ (J g ⁻¹)	ΔS ₃ (J K ⁻¹ kg ⁻¹)	T _D (K)
Co	246 ^H	4.0 ^H	16.5 ^H	301 ^H	3.0 ^H	10.1 ^H	341 ^H	4.8 ^H	14.0 ^H	~510
	230 ^C	4.4 ^C	18.9 ^C	292 ^C	3.0 ^C	10.4 ^C	339 ^C	5.8 ^C	17.1 ^C	-
Co _{0.5} Ni _{0.5}	228 ^H	3.3 ^H	14.5 ^H	301 ^H	2.7 ^H	9.0 ^H	349 ^H	5.1 ^H	14.6 ^H	~540
	-	-	-	290 ^C	2.6 ^C	9.1 ^C	347 ^C	5.1 ^C	14.7 ^C	-
Ni	216 ^H	0.8 ^H	3.8 ^H	302 ^H	2.7 ^H	8.8 ^H	356 ^H	4.5 ^H	12.6 ^H	~560
	-	-	-	291 ^C	2.7 ^C	9.3 ^C	355 ^C	4.8 ^C	13.5 ^C	-

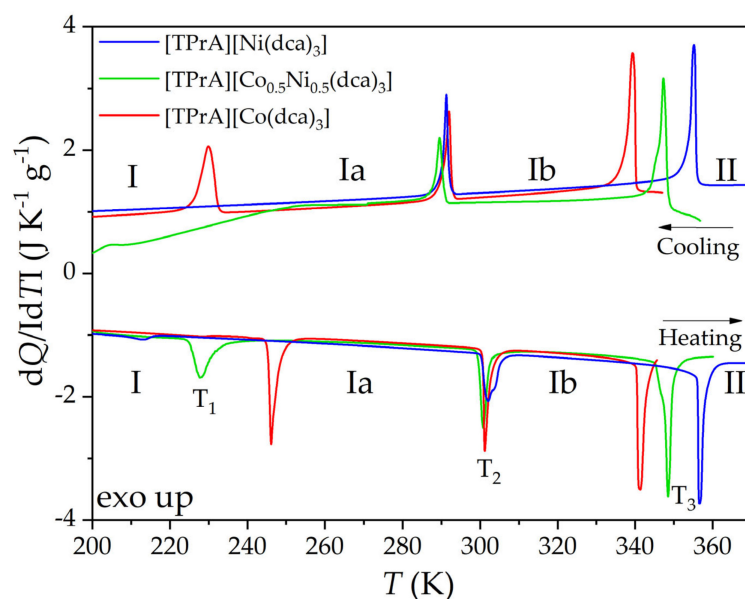


Figure 5. DSC curve of $[\text{TPrA}][\text{Co}_{0.5}\text{Ni}_{0.5}(\text{dca})_3]$ from 200 K to 360 K and comparison with the reported data for $[\text{TPrA}][\text{Co}(\text{dca})_3]$ and $[\text{TPrA}][\text{Ni}(\text{dca})_3]$ (data obtained from Reference [24]).

Taking into account the equation $\Delta S = R \ln(N)$ for an order–disorder transition, where R is the gas constant and N is the ratio of the number of configurations in the disordered and ordered systems, we calculated N as 2.1, 1.6 and 2.0 for the first, second and third transitions, respectively, of the solid solution. These obtained values are consistent with those reported for Co and Ni materials [24].

The TGA curves (Figure 6) show that the thermal behavior of the three compounds is also quite analogous at temperatures higher than 300 K, showing a temperature for the start of the decomposition of the solid solution (~ 540 K) in between the temperatures seen for the parent compounds (~ 510 K for Co and ~ 560 K for Ni) and quite similar steps for the complete decomposition.

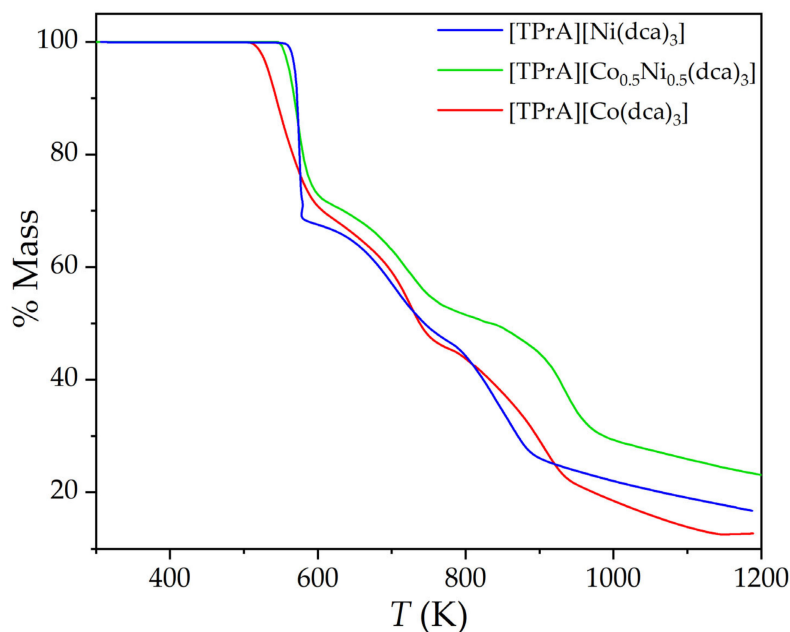


Figure 6. TGA curves of $[\text{TPrA}][\text{Co}_x\text{Ni}_{1-x}(\text{dca})_3]$, where $x = 1.0, 0.5$ and 0.0 , from 300 K to 1200 K.

3.3. Functional Properties

3.3.1. Dielectric Properties

Figure 7 shows the temperature dependence of the real part of the complex dielectric permittivity, ϵ_r' , or dielectric constant, of $[\text{TPrA}][\text{Co}_{0.5}\text{Ni}_{0.5}(\text{dca})_3]$ and a comparison with the parent compounds.

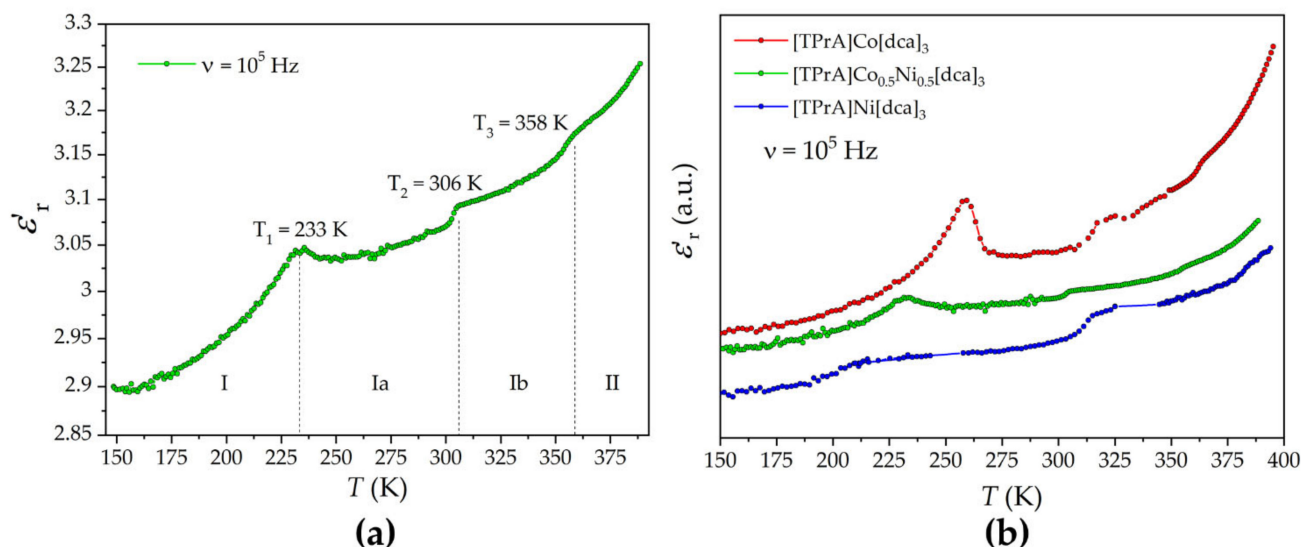


Figure 7. (a) Dielectric constant of the $[\text{TPrA}][\text{Co}_{0.5}\text{Ni}_{0.5}(\text{dca})_3]$ material during heating from 148 K to 390 K. (b) Dielectric constant comparison between $[\text{TPrA}][\text{Co}_x\text{Ni}_{1-x}(\text{dca})_3]$, where $x = 1.0, 0.5$ and 0.0 .

The dielectric behavior of the solid solution seems to fit quite well between that of the parent compounds. Three maxima (or irregularities) of the dielectric constant are clearly observed for $[\text{TPrA}][\text{Co}_{0.5}\text{Ni}_{0.5}(\text{dca})_3]$ at temperatures $T_1 = 233$ K, $T_2 = 306$ K and $T_3 = 358$ K, close to the three solid–solid transitions identified by differential scanning calorimetry during heating. The first dielectric transition clearly appears at 233 K; however, the second and third transitions show a step-like aspect, the most common in this type of material.

3.3.2. Optical Properties

Diffuse reflectance spectra were recorded for $[\text{TPrA}][\text{Co}(\text{dca})_3]$, $[\text{TPrA}][\text{Ni}(\text{dca})_3]$ and $[\text{TPrA}][\text{Co}_{0.5}\text{Ni}_{0.5}(\text{dca})_3]$ solid solutions from 250 to 800 nm and are compared in Figure 8. Below 330 nm, intense bands are observed for all materials due to matrix absorption. In the 330–800 nm range, characteristic d-d absorption bands from the metal ions allow the optical characterization of the hybrids. Very interestingly, $[\text{TPrA}][\text{Co}_{0.5}\text{Ni}_{0.5}(\text{dca})_3]$ shows an absorption spectrum that is a combination (or the overlap) of the spectra of the parent compounds. For $[\text{TPrA}][\text{Co}(\text{dca})_3]$, three absorption maximums are observed at 484, 523 and 613 nm, which were assigned to the transitions from the ground state $^4T_1(\text{F})$ to the excited states $^4T_1(\text{P})$, $^2T_2(\text{G})$, 2E and $^2T_1(\text{G})$ [31]. The first two transitions produce intense, slightly overlapping bands, while the last two appear as a weak overlapping shoulder, partially concealed by previous bands. For $[\text{TPrA}][\text{Ni}(\text{dca})_3]$, four distinct bands were recorded at 388, 458, 635 and 723 nm and were assigned to the absorptions from the ground state $^3A_{2g}(\text{F})$ to the excited states $^3T_{1g}(\text{P})$ and $^4T_{1g}(\text{F})$ [31]. They are both split due to symmetry loss (see Table S3).

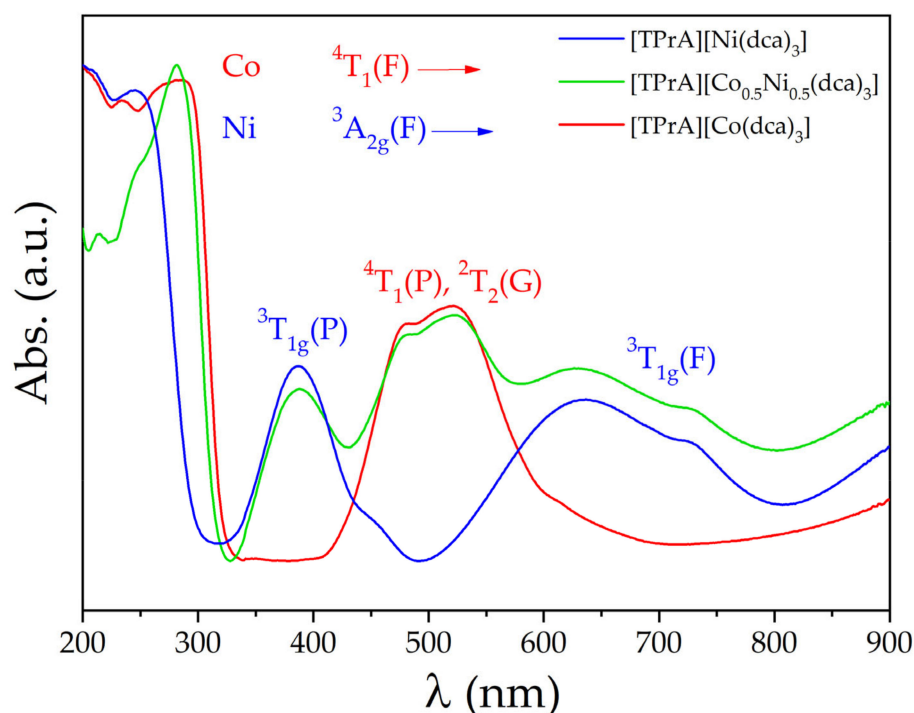


Figure 8. UV-Vis spectra of $[\text{TPrA}][\text{Co}_x\text{Ni}_{1-x}(\text{dca})_3]$, where $x = 1.0, 0.5$ and 0.0 , between 200 and 900 nm.

These results open the possibility of modulating optical properties, such as the optical band gap, just by adjusting the Ni:Co ratio of these solid solutions [32].

3.4. Precursor Materials for CNTs

After the calcination of $[\text{TPrA}][\text{Co}_{0.5}\text{Ni}_{0.5}(\text{dca})_3]$ at 900°C under a nitrogen atmosphere, we obtained black ashes, which are easily attracted to an applied magnet and indicate the presence of magnetic particles.

Figure 9 shows the powder X-ray diffraction pattern of the calcinated sample compared with those obtained from the parent compounds [29]. The most intense and sharp maxima are due to the crystalline structure of Ni/Co metals (COD data sheets 00-210-0649 and 00-900-8492, respectively). As these maxima are not split in the Ni:Co = 1:1 compound, and there is a regular displacement of the position of the maxima towards larger angles as the amount of nickel increases, we conclude that, at least at the scale at which PXRD provides information, the obtained compound from the calcination of mixed cations perovskite is a Ni:Co alloy (or, in other words, a solid solution).

Additionally, the PXRD patterns show a small and wide peak at approximately 26° , which is characteristic of the (002) crystallographic planes of graphite.

To deepen the characterization of the calcined sample, we carried out a study of the obtained ashes using different techniques of electron microscopy, see Figure 10. By means of TEM, we observed the presence of nanostructures in the form of carbon nanotubes with embedded metal nanoparticles (Figure 9). Studies by means of SEM and EDS (see Figure S7) show a homogeneous distribution of Co and Ni in the ashes and an almost equal percentage of both metals (53% Co and 47% Ni). These results are in agreement with our previous results on Ni and Co nanoparticles embedded in CNTs from the calcination of the parent compounds [29]. In addition, we found that the calcination of the hybrid solid solution yields nanoparticles of a fairly homogeneous alloy of metals, also embedded in CNTs.

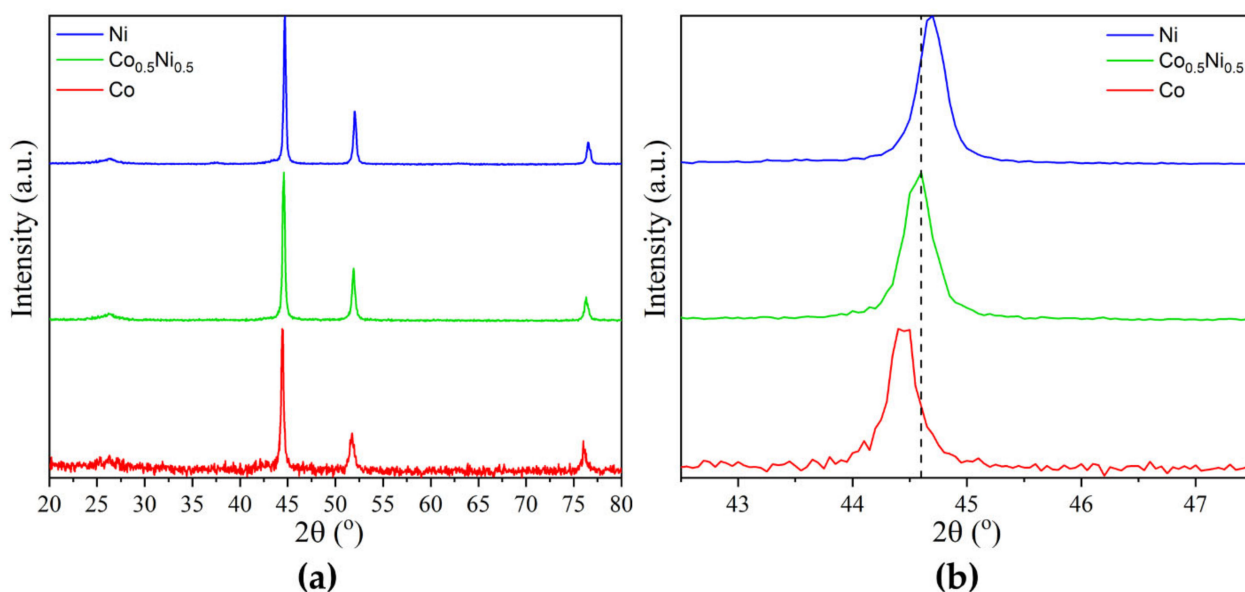


Figure 9. (a) Powder X-ray diffraction patterns obtained after the calcination of $[\text{TPrA}][\text{Co}_x\text{Ni}_{1-x}(\text{dca})_3]$ where $x = 1.0, 0.5, 0.0$. (b) Detail in the region of the maximum intensity peak.

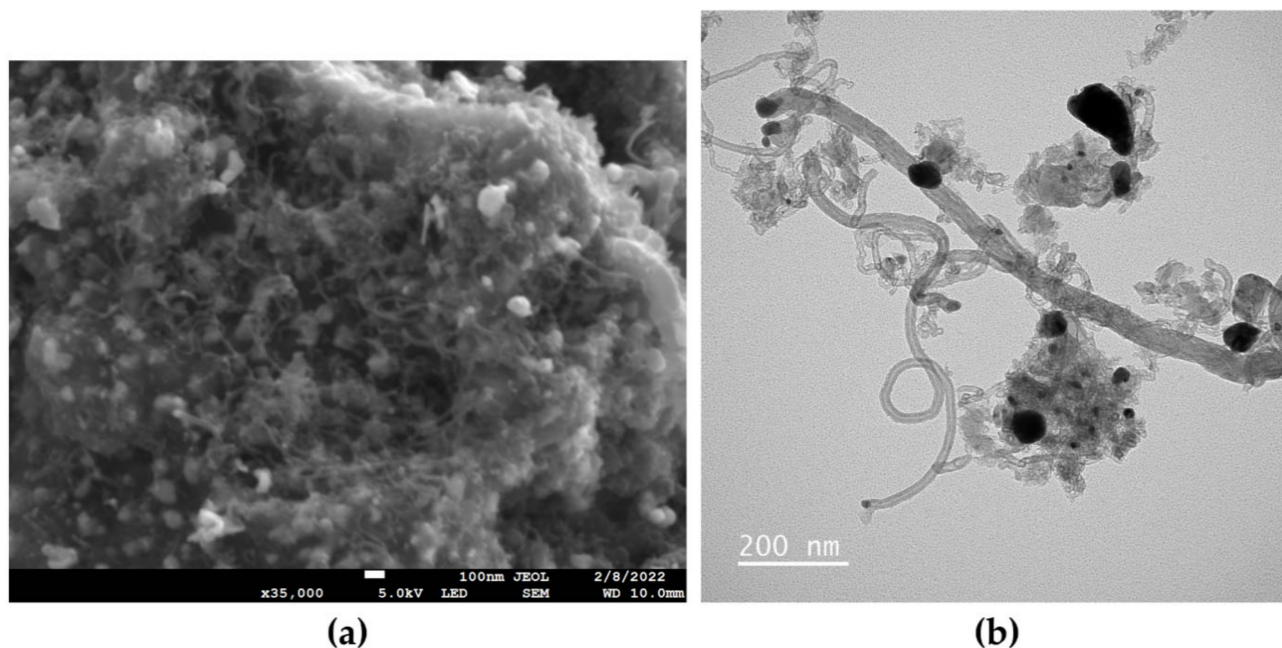


Figure 10. (a) SEM and (b) TEM images of the product obtained by the calcination of the $[\text{TPrA}][\text{Co}_{0.5}\text{Ni}_{0.5}(\text{dca})_3]$ precursor.

Therefore, the simple calcination of the obtained mixed cation compound is an easy route for the preparation of nanostructured magnetic alloys with multiple and interesting applications.

4. Conclusions

Since the growth of interest in hybrid organic–inorganic perovskites (HOIPs) in the last several years, these materials have been subjected to intensive study due to the enormous interest in their functional properties. An attractive option to obtain new compounds and modulate their properties is that of forming solid solutions, a strategy widely used in the case of classical inorganic perovskites but relatively unknown for HOIPs.

In this work, we present the first dicyanamide-perovskite solid solution of [TPrA][Co_{0.5}Ni_{0.5}(dca)₃] and study its functional, thermal, dielectric and optical properties, comparing them with those of the undoped parent compounds [TPrA][Co(dca)₃] and [TPrA][Ni(dca)₃].

In the case of its thermal properties, we observed that the transition temperatures were modified as a function of the Co:Ni proportion. Meanwhile, the enthalpy and entropy values remained similar, except for the low-temperature transition in the Ni compound, which was noticeably lower than in the other two. In addition, the thermal stability of the three compounds seems to be modulated by the metal content, as the 100% Ni compound remained stable up to ~560 K, and the 50:50 solid solution was stable up to ~540 K, while the 100% Co compound was only stable up to ~510 K. The dielectric transitions associated with each of the structural phase transitions were similarly displaced. On the other hand, the absorption spectrum of [TPrA][Co_{0.5}Ni_{0.5}(dca)₃] was a combination (or overlap) of the parent compounds of both full Ni and Co materials.

Therefore, this work confirms that traditional material design strategies, such as solid solutions, used in classic perovskites are also applicable to emerging hybrid perovskites, which will help toward realizing more rational tunability of their functional properties.

Finally, we show that the here-prepared solid solution hybrid compound can be used as a precursor that, upon calcination, gives rise to CNTs with embedded magnetic Ni:Co alloy nanoparticles, a fast and much simpler synthetic route than other complex CVD or arc-discharge methods used to obtain this type of material.

Supplementary Materials: The following are available online at <https://www.mdpi.com/article/10.3390/cryst12060860/s1>. Figure S1: Synthesis scheme of [TPrA][Co_{0.5}Ni_{0.5}(dca)₃] by slow evaporation; Figure S2: (a) scanning electron microscopy image of [TPrA][Co_{0.5}Ni_{0.5}(dca)₃] and X-ray map of (b) carbon, (c) nitrogen, (d) cobalt and (e) nickel; Figure S3: EDS spectrum of [TPrA][Co_{0.5}Ni_{0.5}(dca)₃]; Figure S4: Le Bail refinements of (a) [TPrA][Co(dca)₃], (b) [TPrA][Co_{0.5}Ni_{0.5}(dca)₃] and (c) [TPrA][Ni(dca)₃]; Figure S5: Details of the DSC of [TPrA][Co(dca)₃], [TPrA][Co_{0.5}Ni_{0.5}(dca)₃] and [TPrA][Ni(dca)₃] from (a) 200 K to 260 K, (b) 280 K to 310 K and (c) 330 K to 365 K; Figure S6: Dependence of the transition temperature observed by DSC (by heating) on the metal proportion for the samples [TPrA][Co(dca)₃], [TPrA][Co_{0.5}Ni_{0.5}(dca)₃] and [TPrA][Ni(dca)₃]; Figure S7: EDS spectrum of the CNTs obtained with the calcination of [TPrA][Co_{0.5}Ni_{0.5}(dca)₃]; Table S1: Crystal data and structure refinement for [TPrA][Co_{0.5}Ni_{0.5}(dca)₃]; Table S2: Bond lengths of M-N; Table S3: UV-Vis bands of [TPrA][Co_xNi_{1-x}(dca)₃] (x = 1.0, 0.5, 0.0).

Author Contributions: Conceptualization and methodology, J.G.-B., M.S.-A., J.M.B.-G. and M.A.S.-R.; formal analysis, investigation, data curation and draft writing, J.G.-B., J.S.-B., I.D.-F., P.D.-R., J.L.-B., R.A., S.C.-G., M.S.-A., J.M.B.-G. and M.A.S.-R.; supervision, M.S.-A., J.M.B.-G. and M.A.S.-R. All authors have read and agreed to the published version of the manuscript.

Funding: This work was financially supported by Ministerio de Economía y Competitividad MINECO and EU-FEDER (projects MAT2017-86453-R and PDC2021-121076-I00) and Xunta de Galicia. Funding for the open-access fee was provided by Universidade da Coruña/CISUG.

Institutional Review Board Statement: Not applicable.

Informed Consent Statement: Not applicable.

Data Availability Statement: All data are available from the authors by request.

Acknowledgments: M.A.S.-R. sincerely thanks Emilio Morán Miguélez for all of his teaching, advice, support, friendship and vital optimism during her Ph.D period in Madrid, as well as throughout the years. We will always remember him with gratitude and with a big smile. From the financial point of view, the authors are thankful for financial support from Ministerio de Economía y Competitividad MINECO and EU-FEDER (projects MAT2017-86453-R and PDC2021-121076-I00) and Xunta de Galicia for the collaboration agreement “Development of research strategic actions UDC I + D + i 2021–2022: CICA-Disrupting Projects 2021SEM-A3 (NanoCool)”. J.G.-B. and J.M.B.-G. acknowledge Xunta de Galicia for Predoctoral and Postdoctoral Fellowships, respectively. I.D.-F thanks Ministerio

de Universidades for an FPU Predoctoral Fellowship. The authors also thank Universidade da Coruña/CISUG for funding for the open access of this manuscript.

Conflicts of Interest: The authors declare that they have no known competing financial interests or personal relationships that could have appeared to influence the work reported in this paper.

References

1. Li, W.; Wang, Z.; Deschler, F.; Gao, S.; Friend, R.H.; Cheetham, A.K. Chemically Diverse and Multifunctional Hybrid Organic-Inorganic Perovskites. *Nat. Rev. Mater.* **2017**, *2*, 16099. [[CrossRef](#)]
2. Saparov, B.; Mitzi, D.B. Organic-Inorganic Perovskites: Structural Versatility for Functional Materials Design. *Chem. Rev.* **2016**, *116*, 4558–4596. [[CrossRef](#)] [[PubMed](#)]
3. Jain, P.; Dalal, N.S.; Toby, B.H.; Kroto, H.W.; Cheetham, A.K. Order-Disorder Antiferroelectric Phase Transition in a Hybrid Inorganic-Organic Framework with the Perovskite Architecture. *J. Am. Chem. Soc.* **2008**, *130*, 10450–10451. [[CrossRef](#)] [[PubMed](#)]
4. Jain, P.; Ramachandran, V.; Clark, R.J.; Zhou, H.D.; Toby, B.H.; Dalal, N.S.; Kroto, H.W.; Cheetham, A.K. Multiferroic Behavior Associated with an Order-Disorder Hydrogen Bonding Transition in Metal-Organic Frameworks (MOFs) with the Perovskite ABX₃ Architecture. *J. Am. Chem. Soc.* **2009**, *131*, 13625–13627. [[CrossRef](#)]
5. Sánchez-Andújar, M.; Presedo, S.; Yáñez-Vilar, S.; Castro-García, S.; Shamir, J.; Señarís-Rodríguez, M.A. Characterization of the Order-Disorder Dielectric Transition in the Hybrid Organic-Inorganic Perovskite-like Formate Mn(HCOO)₃[(CH₃)₂NH₂]. *Inorg. Chem.* **2010**, *49*, 1510–1516. [[CrossRef](#)] [[PubMed](#)]
6. Maćzka, M.; Gağor, A.; Ptak, M.; Paraguassu, W.; Da Silva, T.A.; Sieradzki, A.; Pikul, A. Phase Transitions and Coexistence of Magnetic and Electric Orders in the Methylhydrazinium Metal Formate Frameworks. *Chem. Mater.* **2017**, *29*, 2264–2275. [[CrossRef](#)]
7. Hughey, K.D.; Clune, A.J.; Yokosuk, M.O.; Li, J.; Abhyankar, N.; Ding, X.; Dalal, N.S.; Xiang, H.; Smirnov, D.; Singleton, J.; et al. Structure-Property Relations in Multiferroic [(CH₃)₂NH₂] M(HCOO)₃ (M = Mn, Co, Ni). *Inorg. Chem.* **2018**, *57*, 11569–11577. [[CrossRef](#)]
8. Lee, M.M.; Teuscher, J.; Miyasaka, T.; Murakami, T.N.; Snaith, H.J. Efficient Hybrid Solar Cells Based on Meso-Superstructured Organometal Halide Perovskites. *Science* **2012**, *338*, 643–647. [[CrossRef](#)]
9. Burschka, J.; Pellet, N.; Moon, S.-J.; Humphry-Baker, R.; Gao, P.; Nazeeruddin, M.K.; Grätzel, M. Sequential Deposition as a Route to High-Performance Perovskite-Sensitized Solar Cells. *Nature* **2013**, *499*, 316–319. [[CrossRef](#)]
10. Bermúdez-García, J.M.; Sánchez-Andújar, M.; Castro-García, S.; López-Beceiro, J.; Artiaga, R.; Señarís-Rodríguez, M.A. Giant Barocaloric Effect in the Ferroic Organic-Inorganic Hybrid [TPrA][Mn(dca)₃] Perovskite under Easily Accessible Pressures. *Nat. Commun.* **2017**, *8*, 15715. [[CrossRef](#)]
11. Salgado-Beceiro, J.; Nonato, A.; Silva, R.X.; García-Fernández, A.; Sánchez-Andújar, M.; Castro-García, S.; Stern-Taulats, E.; Señarís-Rodríguez, M.A.; Moya, X.; Bermúdez-García, J.M. Near-Room-Temperature Reversible Giant Barocaloric Effects in [(CH₃)₄N]Mn[N₃]₃ Hybrid Perovskite. *Mater. Adv.* **2020**, *1*, 3167–3170. [[CrossRef](#)]
12. Li, J.; Barrio, M.; Dunstan, D.J.; Dixey, R.; Lou, X.; Tamarit, J.L.; Phillips, A.E.; Lloveras, P. Colossal Reversible Barocaloric Effects in Layered Hybrid Perovskite (C₁₀H₂₁NH₃)₂MnCl₄ under Low Pressure Near Room Temperature. *Adv. Funct. Mater.* **2021**, *31*, 2105154. [[CrossRef](#)]
13. Galasso, F.S. *Structure, Properties and Preparation of Perovskite-Type Compounds*; Pergamon Press: Oxford, UK, 1969; ISBN 9780080127446.
14. Rao, C.N.R. *Chemistry of High Temperature Superconductors*; World Scientific: Singapore, 1991; ISBN 978-981-02-0805-9.
15. Rao, C.N.R.; Raveau, B. *Colossal Magnetoresistance, Charge Ordering and Related Properties of Manganese Oxides*; World Scientific: Singapore, 1998; ISBN 978-981-02-3276-4.
16. Weber, O.J.; Charles, B.; Weller, M.T. Phase Behaviour and Composition in the Formamidinium-Methylammonium Hybrid Lead Iodide Perovskite Solid Solution. *J. Mater. Chem. A* **2016**, *4*, 15375–15382. [[CrossRef](#)]
17. Chen, S.; Shang, R.; Wang, B.W.; Wang, Z.M.; Gao, S. An A-Site Mixed-Ammonium Solid Solution Perovskite Series of [(NH₂NH₃)_x(CH₃NH₃)_{1-x}][Mn(HCOO)₃] (X = 1.00–0.67). *Angew. Chem. Int. Ed.* **2015**, *54*, 11093–11096. [[CrossRef](#)]
18. Drozdowski, D.; Gağor, A.; Stefańska, D.; Zaręba, J.K.; Fedoruk, K.; Maćzka, M.; Sieradzki, A. Three-Dimensional Methylhydrazinium Lead Halide Perovskites: Structural Changes and Effects on Dielectric, Linear, and Nonlinear Optical Properties Entailed by the Halide Tuning. *J. Phys. Chem. C* **2022**, *126*, 1600–1610. [[CrossRef](#)]
19. Wu, Y.; Halat, D.M.; Wei, F.; Binford, T.; Seymour, I.D.; Gaultois, M.W.; Shaker, S.; Wang, J.; Grey, C.P.; Cheetham, A.K. Mixed X-Site Formate-Hypophosphite Hybrid Perovskites. *Chem. A Eur. J.* **2018**, *24*, 11309–11313. [[CrossRef](#)]
20. Donlan, E.A.; Boström, H.L.B.; Geddes, H.S.; Reynolds, E.M.; Goodwin, A.L. Compositional Nanodomain Formation in Hybrid Formate Perovskites. *Chem. Commun.* **2017**, *53*, 11233–11236. [[CrossRef](#)]
21. Li, W.; Stroppa, A.; Wang, Z.-M.; Gao, S. *Hybrid Organic-Inorganic Perovskites*; Wiley-VCH: Weinheim, Germany, 2020; ISBN 978-3-527-34431-4.
22. Rao, C.N.R.; Gopalakrishnan, J. *New Directions in Solid State Chemistry*, 2nd ed.; Cambridge University Press: Cambridge, UK, 1997; ISBN 9780521499071.

23. García-Ben, J.; McHugh, L.N.; Bennett, T.D.; Bermúdez-García, J.M. Dicyanamide-Perovskites at the Edge of Dense Hybrid Organic–Inorganic Materials. *Coord. Chem. Rev.* **2022**, *455*, 214337. [[CrossRef](#)]
24. Bermúdez-García, J.M.; Sánchez-Andújar, M.; Yáñez-Vilar, S.; Castro-García, S.; Artiaga, R.; López-Beceiro, J.; Botana, L.; Alegría, A.; Señaris-Rodríguez, M.A. Multiple Phase and Dielectric Transitions on a Novel Multi-Sensitive [TPrA][M(dca)₃] (M: Fe²⁺, Co²⁺ and Ni²⁺) Hybrid Inorganic–Organic Perovskite Family. *J. Mater. Chem. C* **2016**, *4*, 4889–4898. [[CrossRef](#)]
25. Schlueter, J.A.; Manson, J.L.; Geiser, U. Structural and Magnetic Diversity in Tetraalkylammonium Salts of Anionic M[N(CN)₂]₃ (M = Mn and Ni) Three-Dimensional Coordination Polymers. *Inorg. Chem.* **2005**, *44*, 3194–3202. [[CrossRef](#)]
26. Maćzka, M.; Gagor, A.; Ptak, M.; Stefańska, D.; MacAlik, L.; Pikul, A.; Sieradzki, A. Structural, Phonon, Magnetic and Optical Properties of Novel Perovskite-like Frameworks of TriBuMe[M(dca)₃] (TriBuMe = Tributylmethylammonium; dca = Dicyanamide; M = Mn²⁺, Fe²⁺, Co²⁺, Ni²⁺). *Dalton Trans.* **2019**, *48*, 13006–13016. [[CrossRef](#)] [[PubMed](#)]
27. Zhao, M.M.; Zhou, L.; Shi, P.P.; Zheng, X.; Chen, X.G.; Gao, J.X.; Geng, F.J.; Ye, Q.; Fu, D.W. Halogen Substitution Effects on Optical and Electrical Properties in 3D Molecular Perovskites. *Chem. Commun.* **2018**, *54*, 13275–13278. [[CrossRef](#)]
28. Maćzka, M.; Collings, I.E.; Leite, F.F.; Paraguassu, W. Raman and Single-Crystal X-ray Diffraction Evidence of Pressure-Induced Phase Transitions in a Perovskite-like Framework of [(C₃H₇)₄N][Mn(N(CN)₂)₃]. *Dalton Trans.* **2019**, *48*, 9072–9078. [[CrossRef](#)] [[PubMed](#)]
29. Bermúdez-García, J.M.; Yáñez-Vilar, S.; García-Fernández, A.; Sánchez-Andújar, M.; Castro-García, S.; Mira, J.; Moreira, J.A.; Centeno, T.A.; Señaris-Rodríguez, M.A. A Simple in Situ Synthesis of Magnetic M@CNTs by Thermolysis of the Hybrid Perovskite [TPrA][M(dca)₃]. *New J. Chem.* **2017**, *41*, 3124–3133. [[CrossRef](#)]
30. Shannon, R.D. Revised Effective Ionic Radii and Systematic Studies of Interatomic Distances in Halides and Chalcogenides. *Acta Crystallogr.* **1975**, *32*, 751–767. [[CrossRef](#)]
31. White, W.B.; McCarthy, G.J.; Scheetz, B.E. Optical Spectra of Chromium, Nickel, and Cobalt-Containing Pyroxenes. *Am. Mineral.* **1971**, *56*, 72–89.
32. Kumawat, N.K.; Dey, A.; Kumar, A.; Gopinathan, S.P.; Narasimhan, K.L.; Kabra, D. Band Gap Tuning of CH₃NH₃Pb(Br_{1-x}Cl_x)₃ Hybrid Perovskite for Blue Electroluminescence. *ACS Appl. Mater. Interfaces* **2015**, *7*, 13119–13124. [[CrossRef](#)]